Magneto-ionic control of magnetism using a solid-state proton pump

Aik Jun Tan, Mantao Huang, Can Onur Avci, Felix Büttner, Maxwell Mann, Wen Hu, Claudio Mazzoli, Stuart Wilkins, Harry L. Tuller, Geoffrey S. D. Beach

Magneto-ionic control of magnetism using a solid-state proton pump

Aik Jun Tan[1], Mantao Huang[1], Can Onur Avci [1], Felix Büttner[1,2], Maxwell Mann[1], Wen Hu [2], Claudio Mazzoli[2], Stuart Wilkins[2], Harry L. Tuller[1] and Geoffrey S. D. Beach [1]*

Voltage-gated ion transport as a means of manipulating magnetism electrically could enable ultralow-power memory, logic and sensor technologies. Earlier work made use of electric-field-driven O²⁻ displacement to modulate magnetism in thin films by controlling interfacial or bulk oxidation states. However, elevated temperatures are required and chemical and structural changes lead to irreversibility and device degradation. Here we show reversible and non-destructive toggling of magnetic anisotropy at room temperature using a small gate voltage through H⁺ pumping in all-solid-state heterostructures. We achieve 90° magnetization switching by H⁺ insertion at a Co/GdO$_x$ interface, with no degradation in magnetic properties after >2,000 cycles. We then demonstrate reversible anisotropy gating by hydrogen loading in Pd/Co/Pd heterostructures, making metal–metal interfaces susceptible to voltage control. The hydrogen storage metals Pd and Pt are high spin–orbit coupling materials commonly used to generate perpendicular magnetic anisotropy, Dzyaloshinskii–Moriya interaction, and spin–orbit torques in ferromagnet/heavy-metal heterostructures. Thus, our work provides a platform for voltage-controlled spin–orbitronics.

As complementary metal-oxide semiconductor (CMOS) technologies approach the end of their roadmap, spin-based devices are being widely pursued for the beyond- CMOS era. An essential capability for spin-based computing is an effective means of gating magnetism electrically. A key breakthrough came with the predictions[1–3] and experimental confirmation[4,5] that an electric field at the interface between a transition-metal ferromagnet and an oxide dielectric can modulate magnetic anisotropy. Unfortunately, these effects are small, owing to Coulomb screening in the metal. An alternative approach known as magneto-ionic switching[6–21] relies on electrical gating of a mobile ionic species to modulate the properties of a thin ferromagnetic film. Although ionic switching is inherently slower, the effects can be far larger: reversible magneto-ionic anisotropy modulation by up to 5,000 fJ V⁻¹ m⁻¹ has been reported[7,8], compared to about 10 fJ V⁻¹ m⁻¹ through electric field gating[4]. Magneto-ionic switching is hence well suited for applications in which an effective tuning mechanism is more important than speed, such as in neuromorphic[22,23] and stochastic computing[24].

Most recent efforts have focused on O²⁻ displacement in solid-state heterostructures to reversibly modulate magnetic anisotropy[7–9], exchange bias[11], and magnetization[7–9,12] in magnetic metals and oxides by modifying the interfacial oxygen coordination[7–9] or bulk oxygen content[10–12]. The problem with oxygen-based magneto-ionics is that magnetic property changes are accompanied by chemical and structural changes in the target ferromagnet. This often leads to irreversibility[10] and would be detrimental in devices such as magnetic tunnel junctions whose performance depends critically on the structure and electronic properties of the ferromagnet.

Alternatively, ions from Group I of the periodic table such as Li can be inserted into a target ferromagnet to alter magnetic properties without changing the chemical phase or structure[19–21]. Small ion size and the possibility of super-ionic conduction makes this a promising approach to achieving fast, reversible magnetic property switching, but most Group I ions are incompatible with CMOS,

limiting their viability for practical applications. The exception is H⁺, which is relatively innocuous, and is at the same time the smallest possible ion, making it ideal for inducing rapid electric-field-driven property changes in solid-state structures.

Here we show that H_2O hydrolysis in ambient atmosphere (see Methods) catalysed by a rare-earth-oxide/noble-metal interface can serve as a solid-state proton pump that enables non-destructive magnetic property gating with a modest voltage. We demonstrate reversible 90° magnetization switching in a thin Co film at room temperature (25 °C) by either inserting H⁺ at its interface with an oxide or loading hydrogen into an adjacent heavy-metal layer. The mechanism permits both unipolar toggle switching and nonvolatile state retention, with no discernible irreversibility in magnetic properties of the ferromagnet after >2,000 cycles. Moreover, since heavy metals like Pt and Pd that exhibit strong spin–orbit coupling are also well known hydrogen storage materials[25,26] that can be driven between a metal and metal-hydride phase, a host of spin–orbit-induced phenomena at heavy-metal/ferromagnetic interfaces[27–29] becomes accessible to voltage gating despite the fact that electric fields cannot be directly applied.

Co redox through water electrolysis

Figure 1 shows the effect of applying a gate bias to Pt/Co/GdO$_x$/Au under several atmospheric conditions, demonstrating the critical role of ambient moisture in magneto-ionic control of Co oxidation state and magnetic properties. We used a sample structure Ta(4 nm)/Pt(3 nm)/Co(0.9 nm)/GdO$_x$(30 nm)/Au(3 nm) sputter deposited on thermally oxidized Si, with the initial state of the Co layer being either metallic or oxidized as shown in Fig. 1a and b. The oxidized state was induced by reactive sputtering under an oxygen partial pressure P_{O_2} (see Methods). A gate voltage (V_G) was applied to the top Au while the bottom Pt was grounded. The out-of-plane and in-plane magnetization was monitored electrically through the anomalous Hall effect (AHE) and planar Hall effect (PHE), respectively, using a Hall bar geometry (Fig. 1c).
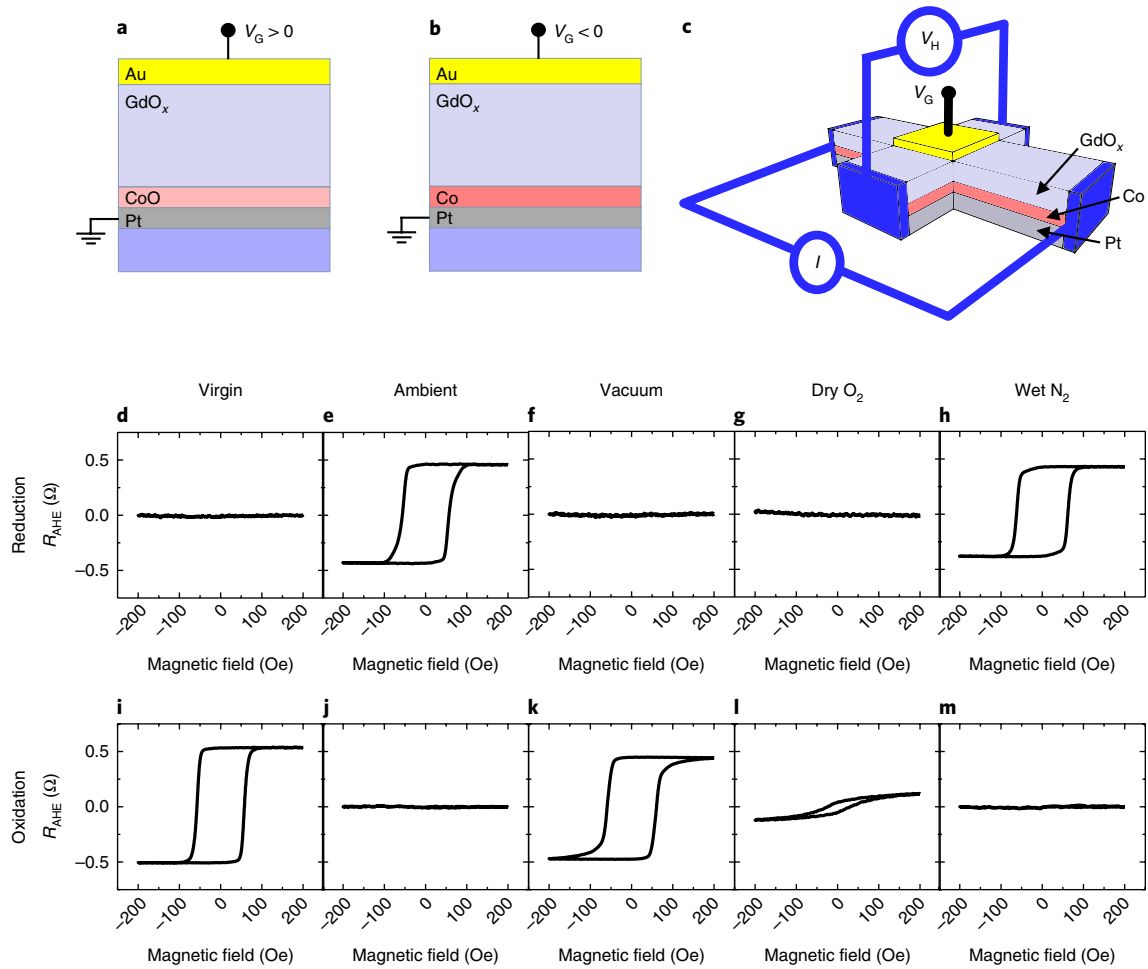
Fig. 1 | In situ probing of magneto-ionic switching in different atmospheres. a, **b**, Active region of a Pt/CoO/GdO$_x$ (**a**) and Pt/Co/GdO$_x$ (**b**) device.
c, Hall cross geometry used for AHE measurement to probe out-of-plane magnetization. V_H is the measured Hall voltage while I is the source current.
d, AHE hysteresis loop of virgin structure in **a**. **e–h**, Hysteresis loops after applying a gate voltage $V_G = +3$ V for 1,000 s under ambient conditions (**e**), under
vacuum (**f**), under dry O$_2$ (**g**) and under wet N$_2$ (**h**). **i**, Hysteresis loop of virgin structure in **b**. **j–m**, Hysteresis loops after applying gate voltage $V_G = -3$ V
for 1,000 s under ambient conditions (**j**), under vacuum (**k**), under dry O$_2$ (**l**) and under wet N$_2$ (**m**).

Figure 1d–h shows out-of-plane hysteresis loops probed through the AHE resistance (R_{AHE}) for the initially oxidized sample. Results are shown for the virgin state (Fig. 1d) and after applying $V_G = +3$ V for 1,000 s at room temperature under various atmospheres (Fig. 1e–h). Consistent with the literature[7,8], under ambient atmosphere, a positive bias results in the appearance of out-of-plane magnetization, corresponding to the reduction of nonmagnetic CoO$_x$ to metallic Co with perpendicular magnetic anisotropy (PMA) (Fig. 1e). Surprisingly, V_G has no effect under vacuum (Fig. 1f), even though a lower-p_{O_2} environment should make oxygen extraction more favourable. Likewise, in dry O$_2$ (Fig. 1g), no magnetic changes are observed, but remarkably, under wet N$_2$ (Fig. 1h), positive V_G leads to the appearance of PMA, implying water-assisted reduction of CoO$_x$ to Co.

Figure 1i–m shows corresponding results for voltage-gated Co oxidation. Under ambient conditions, the AHE signal in the Co layer (Fig. 1i) vanishes after applying $V_G = -3$ V for 1,000 s (Fig. 1j). Since there is no corresponding onset of a PHE signal (not shown), which would be present if the magnetization simply reoriented in-plane, we infer that the Co is oxidized to form non-magnetic CoO$_x$. Under vacuum, voltage gating has no effect (Fig. 1k), which taken alone would suggest that oxidation occurs through O^{2-} pumping from an atmospheric reservoir. However, under a pure O$_2$ environment

(Fig. 1l), voltage-driven oxidation is slower than in ambient, whereas in oxygen-free wet N$_2$ (Fig. 1m) it is faster.

These results imply that the widely assumed mechanism of magneto-ionic switching through electric-field-driven oxygen displacement[7,8,10,11] is incomplete, and that H$_2$O plays an essential role. It is well known that the water splitting reaction can be catalysed by noble metals with oxide support[30–32]. Water splitting and hydrogen incorporation have been shown to substantially affect the switching behaviour and electronic properties in metal/oxide/metal memristors[33–35]. Similar reactions in the present Pt/Co/GdO$_x$/Au stacks would provide a simple, self-consistent explanation of the results in Fig. 1.

During reduction of CoO$_x$ under positive V_G, we propose that H$_2$O is hydrolysed at the top electrode, producing H$^+$ and O$_2$ through the oxygen evolution reaction[31]. The proton is transported to the bottom electrode via a Grotthuss-type mechanism[36–38] in which the H$^+$ ion hops from an OH$^-$ to the adjacent O^{2-} ion, enabled by solid-state dissolution of water in the oxide matrix[39] (see Supplementary Information section 3). At the bottom electrode, the proton reacts with CoO to form Co and H$_2$O. The net reactions, depicted in Fig. 2a, are:

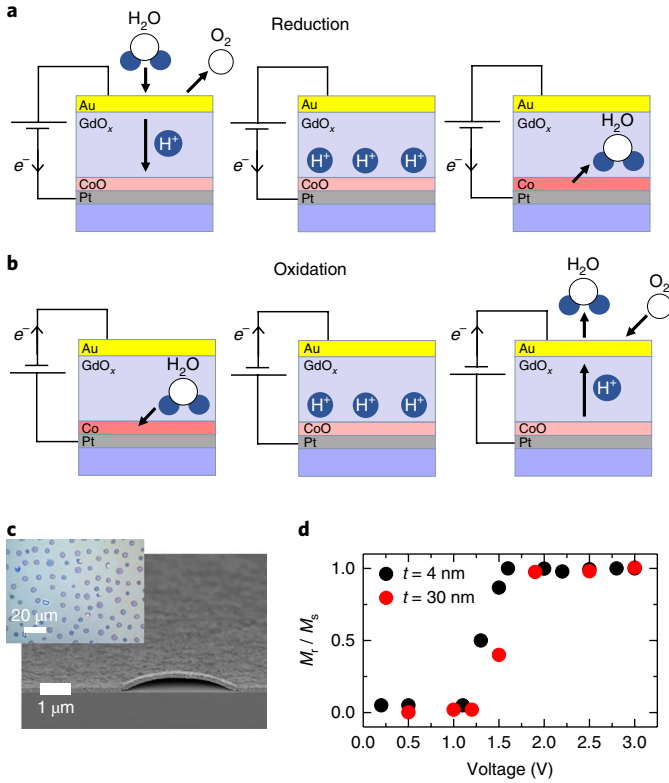$$\text{Anode (Au):} \quad 2H_2O \rightarrow 4H^+ + O_2 + 4e^- \tag{1}$$
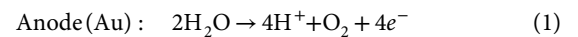
Fig. 2 | Electrochemical reactions in a magneto-ionic cell. a, Schematic of CoO reduction at gate voltage $V_G > 0$ involving H_2O hydrolysis. **b**, Schematic of Co oxidation at gate voltage $V_G < 0$ involving H_2O recombination. **c**, Cross-sectional scanning electron microscope image of a Pt(3 nm)/GdO$_x$(100 nm)/Au(3 nm) device after $V_G = +3$ V has been applied for 5 h. The inset shows an optical micrograph of the device. Hydrogen gas is produced between the Pt and GdO$_x$ layer at the end of the experiment. **d**, Out-of-plane remanent magnetization ratio M_r/M_s of Pt(3 nm)/Co(0.9 nm)/GdO$_x$(t_{GdO_x})/Au(3 nm) structure after applying various V_G for >5 h, for $t_{GdO_x} = 4$ nm and 30 nm.

$$\text{Cathode (Pt)}: \quad 4H^+ + 2Co^{2+} + 2O^{2-} + 4e^- \rightarrow 2H_2O + 2Co \quad (2)$$
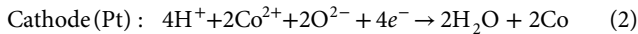
The water evolved at the bottom electrode can either be stored in grain boundaries, or is more likely to be incorporated into GdO$_x$ itself as hydroxide, namely through the reaction[40] $Gd_2O_3 + 3H_2O \rightarrow 2Gd(OH)_3$. Co oxidation under negative V_G occurs by the reverse process (Fig. 2b), with Pt acting as the anode for Co oxidation and Au acting as the cathode for H_2O recombination (see Supplementary Information section 4). In both the oxidation and reduction process, it is expected that mass transport is dominated by protons instead of O^{2-} owing to the much smaller size and lower activation energy for hopping of the former[38].

If positive V_g pumps H^+ as proposed, sustained bias application should lead to hydrogen accumulation and evolution at the bottom electrode, and this is indeed observed. Figure 2c shows a scanning electron microscope image of a Pt(3 nm)/GdO$_x$(100 nm)/Au(3 nm) film after applying $V_G = +3$ V for 5 h. The inset optical micrograph shows bubble formation, which after cross-sectioning is revealed to arise from gas evolution and GdO$_x$ delamination at the bottom electrode, which could only be H_2 since O_2 evolution could only occur at the anode. Formation of H_2 bubbles under similar conditions has also been recently observed in Pt/TiO$_{2-x}$/Pt memristors[35].

Figure 2d shows the voltage threshold for the onset of PMA in a CoO structure to be about 1.5 V, which agrees well with the

proposed reactions in equations (1) and (2)[31]. This threshold is independent of GdO$_x$ thickness t_{GdO_x}, as seen in Fig. 2d, implying that the process is dictated by an electrochemical reaction rather than by an electric field. Cyclic voltammetry measurements (Supplementary Fig. 4f and g) provide further support for the proposed reaction chemistry[41].

Magnetic anisotropy control by proton injection

We now show that hydrogen insertion at the Co/GdOx interface allows the anisotropy to be toggled from out-of-plane to in-plane without requiring redox reactions in the ferromagnetic Co (Fig. 3a). Surface anisotropy is known to be sensitive to adsorbed H, as shown previously for ultrathin ferromagnetic films in ultrahigh vacuum upon exposure to molecular or atomic hydrogen[42,43]. Here, we show that the same behaviour can be gated in solid-state devices. Starting from a virgin state with PMA (Fig. 3b), the magnetization rotates in-plane when $V_G = +3$ V is applied for 800 s (Fig. 3c), corresponding to accumulation of hydrogen at the Co/GdO$_x$ interface. When V_G is set to 0 V (grounded), PMA is spontaneously recovered (Fig. 3d) as the accumulated hydrogen forms H^+ and diffuses away from the bottom electrode. In-plane magnetization reorientation is confirmed by Fig. 3e–g, which shows that the PHE signal is absent when the film has PMA and is present when the AHE signal vanishes (Fig. 3e–g) under positive bias. Similar to the reduction of CoO described above, the accumulation of hydrogen that causes this magnetization reorientation transition only occurs in the presence of humidity, as shown in Supplementary Fig. 7.

Figure 3h–j shows cycling results for a device with $t_{GdO_x} = 4$ nm, in which switching is much faster. V_G was cycled >2,000 times between +3 V and 0 V at 0.5 Hz, and out-of-plane hysteresis loops were acquired at 25-ms intervals using a polar magneto-optical Kerr effect (MOKE) polarimeter (see Methods). Figure 3h shows the ratio of the remanent (M_r) to saturation magnetization (M_s) as a function of time, for cycles 1–10 and 2,060–2,070, tracking the in-plane/out-of-plane transitions (Fig. 3i). The square out-of-plane loop in the virgin state (Fig. 3i) is indistinguishable from the loop after toggling the magnetization in plane, both after the first cycle (Fig. 3i) and after cycle 2,070 (Fig. 3j). We find, however, that the response time degrades slightly with repeated cycling (Fig. 3h), which may be associated with increased leakage currents in the oxide. The switching times at the rising and falling V_G edge are 100 ms and 400 ms respectively (Supplementary Fig. 10). This switching speed is faster than any room-temperature results in the literature for magneto-ionic switching[7,8]. The asymmetry in switching can be mitigated by applying a negative V_G to accelerate H^+ removal from the interface, but this can also lead to Co oxidation, which leads to a progressive irreversible degradation of PMA owing to the irreversibility of oxygen insertion into the magnetic layer[10] (Supplementary Figure 9).

The electrochemical reactions at $V_G = +3$ V in the two half cells (top and bottom electrodes), given by:

$$\text{Anode (Au)}: 2H_2O \rightarrow 4H^+ + O_2 + 4e^- \quad (3)$$

$$\text{Cathode (Pt)}: \quad 4H^+ + 4e^- \rightarrow 4H \quad (4)$$
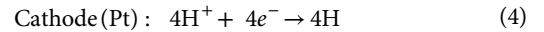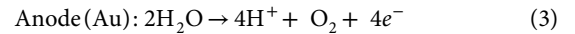
cannot proceed without electron flow through the external circuit. Thus, one can realize two operating modes by either grounding the device ($V_G = 0$ V) or leaving the device at open circuit when V_G is removed. Figure 4a shows that after $V_G = +3$ V is applied, the magnetization transitions from out-of-plane (Fig. 4b) to in-plane (Fig. 4c), and when V_G is set to open circuit, the in-plane state is retained (Fig. 4c and d). This implies that the accumulated hydrogen remains at the interface. In fact, for a device with very low leakage, this hydrogen-loaded state can be retained for more than three days under ambient conditions and at least a week under vacuum,
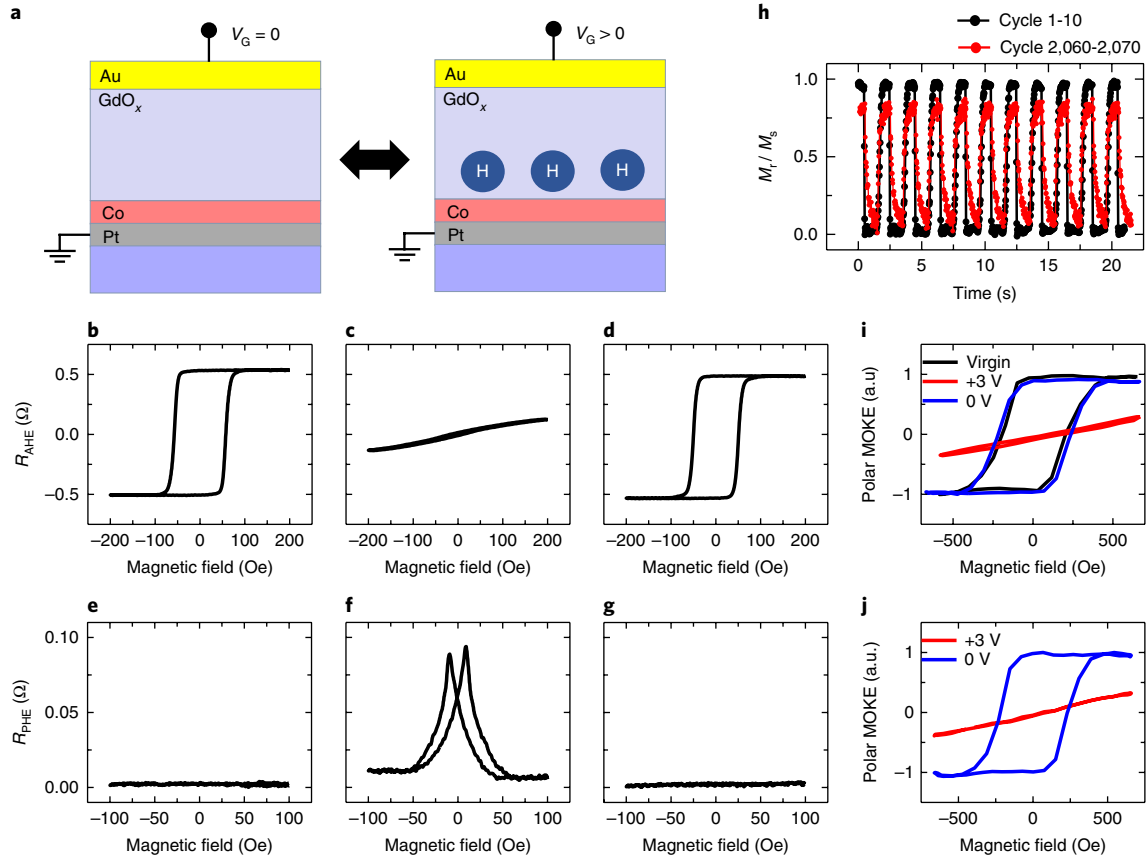
Fig. 3 | Magneto-ionic switching based on hydrogen accumulation at the Co/GdO$_x$ interface. a, Schematic of magneto-ionic switching scheme. H indicates hydrogen at the Co/GdO$_x$ interface. **b–d**, AHE hysteresis loops in the virgin state (**b**), after gate voltage $V_G = +3$ V is applied for 800 s (**c**), and after gate voltage V_G is set to 0 V for 800 s (**d**). **e–g**, PHE hysteresis loops corresponding to **b–d**, respectively. **h**, Out-of-plane magnetization remanence ratio M_r/M_s versus time as V_G is cycled between +3 V and 0 V at 0.5 Hz for 2,070 cycles, extracted from hysteresis loops measured by the polar MOKE. Results are shown for the first and last ten cycles. **i**, Out-of-plane hysteresis loops corresponding to the virgin state and the first switching cycle. **j**, Out-of-plane hysteresis loops corresponding to cycle 2,070. The hysteresis loop of the final relaxed state is identical to that in the virgin state.

as shown in Supplementary Information section 5. When the device is subsequently set to closed circuit, PMA is spontaneously recovered (Fig. 4e). Hence, the magnetization state can be switched in a nonvolatile fashion between the out-of-plane and in-plane states, or toggled with a unipolar voltage, depending on whether the $V_G = 0$ condition is at open or closed circuit. This ability to modify the magnetic state over two very distinct timescales can be particularly attractive for neuromorphic computing where one can modify the memory[22,23] (non-volatile) during computation and once the computation is complete, all memory elements are reinitialized to the same state during a refresh stage (volatile).

These results show that removal of H from the bottom electrode requires the reactions in equations (3) and (4) to occur in reverse. To be removed, H must first split into H$^+$ and e^- at the bottom electrode, so that the H$^+$ can be transported back up through the GdO$_x$ to the top electrode, where it recombines with atmospheric oxygen. If there is no electronic conduction path, the reaction cannot proceed and as a result the in-plane magnetized state is retained at open circuit. Hence, a finite leakage current through the GdO$_x$ reduces the stability of the hydrogen-loaded state (Supplementary Information section 5) under ambient conditions, because it offers an alternate path for electron transfer from the bottom electrode to the top electrode. In Supplementary Information section 5, we also show that, when the device is in vacuum, equation (3) becomes rate-limiting, and the out-of-plane state cannot be recovered even when applying a reverse bias. From this, we conclude that H cannot

simply diffuse from the bottom electrode; its insertion and removal are governed by the anodic and cathodic electrochemical reactions in equations (3) and (4).

Next, to quantify the amount of hydrogen needed to achieve the in-plane state, we also measured the transient (discharge) current flowing in the opposite direction when V_G is set to 0 V, driven by the chemical potential (Nernst potential) that arises in the hydrogen-loaded state. During this measurement, we simultaneously probed the time-dependent Co magnetic orientation (Supplementary Fig. 6). From the integrated charge, we found that approximately 1 H for every 10 Co atoms is needed to retain the in-plane switched state. We note that this value is an upper bound as the amount of hydrogen immediately adjacent to the Co/GdO$_x$ interface may be significantly less than the total amount of hydrogen that is stored in GdO$_x$.

Voltage control of a heavy-metal/ferromagnet interface

Since Pd is well known for its hydrogen loading capacity[25], and atmospheric hydrogen loading in Pd/Co/Pd has previously been shown to modulate PMA[43], we next exploit this feature by inserting a Pd layer between Co and GdO$_x$. Figure 5a shows the layer schematic of a Ta(4 nm)/Pd(3 nm)/Co(0.6 nm)/Pd(4.5 nm)/GdO$_x$ (10 nm)/Au(3 nm) heterostructure. Because the Co layer is protected by Pd, negative V_G does not result in oxidation of Co (Fig. 5b), which allows for applying a negative gate bias to accelerate H removal and recovery of PMA. In this device, positive and negative V_G can pump hydrogen into and out of the Pd layer reversibly, switching
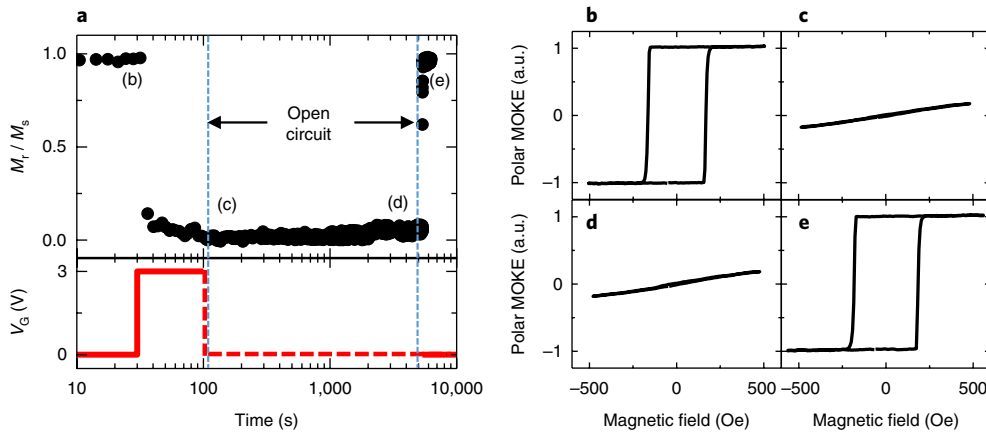
Fig. 4 | Magnetic response under short circuit and open circuit. a, Evolution of out-of-plane magnetization remanence ratio M_r/M_s versus time and the corresponding gate voltage V_G. The dashed line indicates open circuit while the solid line at $V_G = 0$ V indicates short circuit. $V_G = +3$ V is applied between time $t = 30$ s and $t = 100$ s, at which point the probe is lifted from the top electrode. At $t = 5,300$ s, the probe is landed again and V_G set to 0 V (ground). **b–e**, Polar MOKE hysteresis loops corresponding to $t = 25$ s (**b**), $t = 110$ s (**c**), and $t = 4,200$ s (**d**), and $t = 5,600$ s (**e**).

the anisotropy from out-of-plane to in-plane and back[43] (Fig. 5c–e). Figure 5f shows the switching cycles of M_r/M_s as V_G is cycled between +4 V and −1 V at 1 Hz. Robust switching was achieved, with a switching time of around 150 ms at both the rising and falling edges (Supplementary Fig. 11).

To provide direct evidence of insertion of H into the heavy-metal layer, we performed X-ray absorption spectroscopy (XAS) at the 23-ID-1 beamline at the National Synchrotron Light Source II (see Methods). Figure 5g shows an XAS spectrum of a virgin Ta(4 nm)/ Pd(3 nm)/Co(~0.6 nm)/Pd(4.5 nm)/GdO$_x$(30 nm)/Au(3 nm) sample in the range between 525 eV and 575 eV, where one can observe the Pd M$_3$ edge[44] at about 532 eV and O K-edge at about 538 eV. The identity of the Pd M$_3$ peak is verified by measuring the XAS spectrum with and without a Pd layer (Supplementary Fig. 12). Figure 5h shows comparison of the Pd M$_3$ edge in a virgin and in a voltage-modified device. For the voltage-modified device, V$_G$ = +3 V is applied for >5 min ex situ before the XAS spectrum was measured. From the data, we can clearly observe a peak shift of around +0.7 eV for the Pd M$_3$ edge upon voltage application. This shift arises from two sources. First, previous XPS studies have shown that the binding energy of core electrons shifts slightly when Pd becomes PdH$_x$. This shift is around +0.17 eV for the 3d electrons and its magnitude is very small because hydrogen in Pd is well screened in the lattice[45]. Second, there is a change in energy of the final unoccupied 4d states of Pd by around +0.7 eV when it becomes a hydride[46,47]. This change accounts for most of the peak shift in the XAS spectrum. The total peak shift of the Pd M$_3$ edge should therefore be around +0.87 eV, which is very close to the +0.7 eV peak shift we observe in our data. We have also confirmed this with a thick Mg as the hydrogen loading layer[48] and the results show that a substantial amount of hydrogen can be pumped into the system using this mechanism (Supplementary Fig. 13). Thus we have shown that the magnetic anisotropy at a metal/metal interface can be modulated substantially by an electric field through electrochemical gating of a metal to its hydride phase in an appropriately designed solid-state heterostructure. This effect cannot be achieved by any other known mechanism because electric fields vanish in a metal.

Conclusions

We have shown that hydrogen plays an essential part in previously observed magneto-ionic switching. We introduced a new switching scheme based on hydrogen accumulation and removal at a Co/GdO$_x$ interface to achieve excellent cyclability and fast

room-temperature operation. Depending on the application, the device can be operated in a volatile or non-volatile mode, allowing for device toggling or low-power state retention. The anisotropy changes that can be achieved correspond to magnetoelectric efficiencies of at least 5,000 fJ V^{-1} m^{-1} (Supplementary Information section 14), similar to the maximum values reported for oxygen ion gating[7,8], but without the associated change in chemical state. In terms of switching speed, this new mechanism compares favourably to other ionic-mediated gating mechanisms. For instance, lithium intercalation[19,21] takes hours to produce substantial magnetic changes in the device, and while this timescale can be reduced down to tens of minutes by increasing the charging current, this usually comes at the expense of cyclability. For oxygen-ion gating, ref. [9] have demonstrated fast control of magnetism down to about 0.2 ms in a Co/SrCoO$_{2.5}$ heterostructure at room temperature, but they were only able to tune the coercivity by a few oersted, which is too little for practical devices. For oxygen-ion gating in Co/GdO$_x$ stacks, typical response times are of the order of minutes to tens of minutes and the effect usually requires elevated temperatures[7,8]. Our achievement of 100 ms switching at room temperature, with robust behavior for >2,000 cycles, thus holds promise for applications such as neuromorphic computing, where switching rates of the order of 100 Hz can permit practical device implementations[49]. Although device retention at this stage is a few days, we expect substantial improvement with further engineering of the hydrogen storage material. We remark that the non-volatility of the gating effect is not a prerequisite for its utility, as many current proposed applications are based on dynamic modulation of magnetic anisotropy for efficient current-induced switching. Finally, we have also demonstrated voltage gating of a metal/metal interface by harnessing the hydrogen loading capability of noble metals such as Pd in a Pd/Co/Pd/GdO$_x$ heterostructure. This paves the way towards solid-state voltage gating of other spin–orbital and exchange effects mediated by heavy metals with substantial hydrogen storage capacity, such as spin–orbit torques[28], the Dzyaloshinskii–Moriya interaction[27] and RKKY exchange coupling[29] in buried ferromagnet/metal interfaces. Such devices can be implemented by using a symmetric heavy metal/ ferromagnet/heavy metal structure, for instance, where we can generate inversion symmetry by loading hydrogen into one of the heavy-metal layers and in turn completely remove (or restore) the Dzyaloshinskii–Moriya interaction or spin–orbit torques using a gate voltage. Finally, to make this an entirely closed system, a
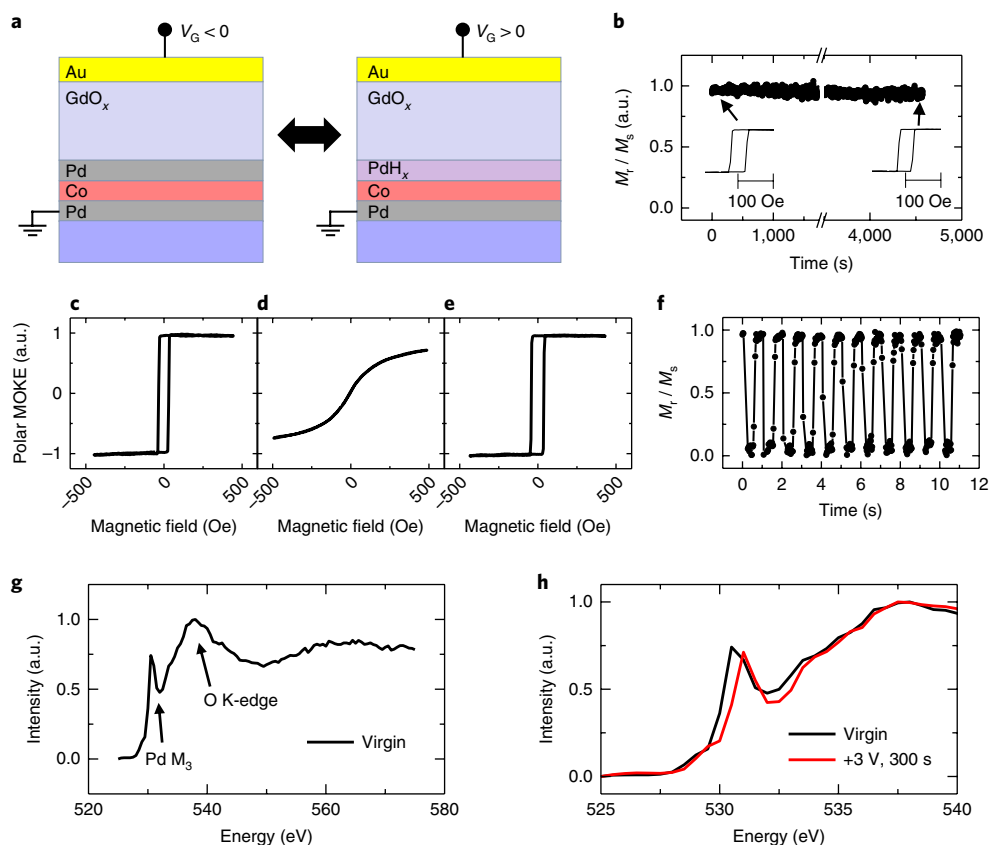
Fig. 5 | Voltage gating of metal/metal interface by exploiting hydrogen loading in Pd. a, Schematic of device operation in a Pd/Co/Pd/GdO$_x$ cell.
b, Out-of-plane magnetization remanence ratio M_r/M_s versus time at gate voltage $V_G = -3$ V. The inset shows the MOKE hysteresis loops at $t = 0$ s and
$t = 4,500$ s. **c-e**, Polar MOKE hysteresis loops corresponding to the virgin state (**c**), after $V_G = +4$ V (**d**), and after V_G is set to -1 V (**e**). **f**, M_r/M_s as V_G is
cycled between $+4$ V and -1 V at 1 Hz. Each data point corresponds to a 25-ms MOKE hysteresis loop. **g**, XAS spectrum of a Pd (3 nm)/Co (0.6 nm)/
Pd (4.5 nm)/GdO$_x$ (30 nm)/Au(3 nm) sample in the range between 525 eV and 575 eV. **h**, XAS of a virgin and voltage-modified ($V_G = +3$ V for >5 min)
sample, clearly indicating an energy shift in the Pd M$_3$ peak for the voltage-modified sample.

hydrogen storage layer[50] such as WO$_3$ can be integrated on top of the GdO$_x$ electrolyte, making it very practical for real devices.

Online content

Any methods, additional references, Nature Research reporting summaries, source data, statements of data availability and associated accession codes are available at https://doi.org/10.1038/s41563-018-0211-5.

References

1. Duan, C. G. et al. Surface magnetoelectric effect in ferromagnetic metal films. *Phys. Rev. Lett.* **101**, 137201 (2008).
2. Tsujikawa, M. & Oda, T. Finite electric field effects in the large perpendicular magnetic anisotropy surface Pt/Fe/Pt(001): a first-principles study. *Phys. Rev. Lett.* **102**, 247203 (2009).
3. Niranjan, M. K., Duan, C. G., Jaswal, S. S. & Tsymbal, E. Y. Electric field effect on magnetization at the Fe/MgO(001) interface. *Appl. Phys. Lett.* **96**, 107–110 (2010).
4. Maruyama, T. et al. *Large voltage-induced magnetic anisotropy change in a few atomic layers of iron. Nat. Nanotech.* **4**, 158–161 (2009).
5. Shiota, Y. et al. Voltage-assisted magnetization switching in ultrathin Fe$_{80}$Co$_{20}$ alloy layers. *Appl. Phys. Express* **2**, 063001 (2009).
6. Bauer, U., Emori, S. & Beach, G. S. D. *Voltage-controlled domain wall traps in ferromagnetic nanowires. Nat. Nanotech.* **8**, 411–416 (2013).
7. Bauer, U. et al. Magneto-ionic control of interfacial magnetism. *Nat. Mater.* **14**, 174–181 (2014).
8. Bi, C. et al. Reversible control of Co magnetism by voltage-induced oxidation. *Phys. Rev. Lett.* **113**, 267202 (2014).
9. Li, H. B. et al. Electric-field control of ferromagnetism through oxygen ion gating. *Nat. Commun.* **8**, 2156 (2017).
10. Gilbert, D. A. et al. Structural and magnetic depth profiles of magneto-ionic heterostructures beyond the interface limit. *Nat. Commun.* **7**, 12264 (2016).
11. Gilbert, D. A. et al. Controllable positive exchange bias via redox-driven oxygen migration. *Nat. Commun.* **7**, 11050 (2016).
12. Grutter, A. J. et al. Reversible control of magnetism in La$_{0.67}$Sr$_{0.33}$MnO$_3$ through chemically-induced oxygen migration. *Appl. Phys. Lett.* **108**, 82405 (2016).
13. Lu, N. et al. Electric-field control of tri-state phase transformation with a selective dual-ion switch. *Nature* **546**, 124–128 (2017).
14. Di, N. et al. Influence of controlled surface oxidation on the magnetic anisotropy of Co ultrathin films. *Appl. Phys. Lett.* **106**, 122405 (2015).
15. Duschek, K., Uhlemann, M., Schlörb, H., Nielsch, K. & Leistner, K. Electrochemical and in-situ magnetic study of iron/iron oxide films oxidized and reduced in KOH solution for magneto-ionic switching. *Electrochem. Commun.* **72**, 153–156 (2016).
16. Walter, J. et al. Ion-gel-gating-induced oxygen vacancy formation in epitaxial La$_{0.5}$Sr$_{0.5}$CoO films from in operando X-ray and neutron scattering. *Phys. Rev. Mater.* **1**, 071403 (2017).
17. Walter, J., Wang, H., Luo, B., Frisbie, C. D. & Leighton, C. Electrostatic versus electrochemical doping and control of ferromagnetism in ion-gel-gated ultrathin La$_{0.5}$Sr$_{0.5}$CoO$_{3-\delta}$. *ACS Nano* **10**, 7799–7810 (2016).
18. Leng, X. et al. Insulator to metal transition in WO3 induced by electrolyte gating. *npj Quantum Mater.* **2**, 35 (2017).
19. Zhang, Q. et al. Lithium-ion battery cycling for magnetism control. *Nano. Lett.* **16**, 583–587 (2016).
20. Zhu, X. et al. In situ nanoscale electric field control of magnetism by nanoionics. *Adv. Mater.* **28**, 7658–7665 (2016).

21. Dasgupta, S. et al. Toward on-and-off magnetism: reversible electrochemistry to control magnetic phase transitions in spinel ferrites. *Adv. Funct. Mater.* **26**, 7507–7515 (2016).
22. Burr, G. W. et al. Neuromorphic computing using non-volatile memory. *Adv. Phys. X* **2**, 89–124 (2017).
23. Pershin, Y. V. & Di Ventra, M. Experimental demonstration of associative memory with memristive neural networks. *Neural Netw.* **23**, 881–886 (2010).
24. Knag, P., Member, S., Lu, W. & Zhang, Z. A native stochastic computing architecture enabled by memristors. *IEEE Trans. Nanotechnol.* **13**, 283–293 (2014).
25. Adams, B. D. & Chen, A. The role of palladium in a hydrogen economy. *Mater. Today* **14**, 282–289 (2011).
26. Schlapbach, L. & Züttel, A. Hydrogen-storage materials for mobile applications. *Nature* **414**, 353–358 (2002).
27. Yang, H., Thiaville, A., Rohart, S., Fert, A. & Chshiev, M. Anatomy of Dzyaloshinskii-Moriya Interaction at Co/Pt Interfaces. *Phys. Rev. Lett.* **115**, 267210 (2015).
28. Hoffmann, A. Spin Hall effects in metals. *IEEE. Trans. Magn.* **49**, 5172–5193 (2013).
29. Parkin, S. S. P., Bhadra, R. & Roche, K. P. Oscillatory magnetic exchange coupling through thin copper layers. *Phys. Rev. Lett.* **66**, 2152–2155 (1991).
30. Campbell, C. T. Catalyst–support interactions: electronic perturbations. *Nat. Chem.* **4**, 597–598 (2012).
31. Rossmeisl, J., Logadottir, A. & Nørskov, J. K. Electrolysis of water on (oxidized) metal surfaces. *Chem. Phys.* **319**, 178–184 (2005).
32. Rodriguez, J. A., Liu, P., Hrbek, J., Evans, J. & Pérez, M. Water gas shift reaction on Cu and Au nanoparticles supported on $Ce_O2(111)$ and ZnO(0001): intrinsic activity and importance of support interactions. *Angew. Chem. Int. Ed.* **46**, 1329–1332 (2007).
33. Valov, I. & Lu, W. D. Nanoscale electrochemistry using dielectric thin films as solid electrolytes. *Nanoscale* **8**, 13828–13837 (2016).
34. Tsuruoka, T. et al. Effects of moisture on the switching characteristics of oxide-based, gapless-type atomic switches. *Adv. Funct. Mater.* **22**, 70–77 (2012).
35. Yin, Q. et al. Cathode bubbles induced by moisture electrolysis in TiO_{2-x}-based resistive switching cells. *J. Phys. D* **49**, 09LT01 (2016).
36. Kreuer, K. Proton conductivity: materials and applications. *Chem. Mater.* **8**, 610–641 (1996).
37. Norby, T., Widerøe, M., Glöckner, R. & Larring, Y. *Hydrogen in oxides. Dalt. Trans.* **0**, 3012–3018 (2004).
38. Shirpour, M., Gregori, G., Merkle, R. & Maier, J. On the proton conductivity in pure and gadolinium doped nanocrystalline cerium oxide. *Phys. Chem. Chem. Phys.* **13**, 937–940 (2011).
39. Bi, L., Boulfrad, S. & Traversa, E. Steam electrolysis by solid oxide electrolysis cells (SOECs) with proton-conducting oxides. *Chem. Soc. Rev.* **43**, 8255–8270 (2014).
40. Cohen, S. et al. The interaction of H_2O with the surface of polycrystalline gadolinium at the temperature range of 300-570 K. *Surf. Sci.* **617**, 29–35 (2013).
41. Stamenkovic, V. R., Strmcnik, D., Lopes, P. P. & Markovic, N. M. Energy and fuels from electrochemical interfaces. *Nat. Mater.* **16**, 57–69 (2017).
42. Sander, D. et al. Reversible H-induced switching of the magnetic easy axis in Ni/Cu(001) thin films. *Phys. Rev. Lett.* **93**, 247203 (2004).
43. Munbodh, K., Perez, F. A., Keenan, C. & Lederman, D. Effects of hydrogen/deuterium absorption on the magnetic properties of Co/Pd multilayers. *Phys. Rev. B* **83**, 94432 (2011).
44. Thompson, A. C. & Vaughn, D. *X-Ray Data Booklet* (Center for X-ray Optics and Advanced Light Source, Berkeley, 2001); http://xdb.lbl.gov
45. Bennett, P. A. & Fuggle, J. C. Electronic structure and surface kinetics of palladium hydride studied with X-ray photoelectron spectroscopy and electron-energy-loss spectroscopy. *Phys. Rev. B* **26**, 6030–6039 (1982).
46. Davoli, I. et al. Palladium L_3 absorption edge of $PdH_{0.6}$ films: evidence for hydrogen induced unoccupied states. *Solid State Commun.* **71**, 383–390 (1989).
47. Tew, M. W., Miller, J. T. & van Bokhoven, J. A. Particle size effect of hydride formation and surface hydrogen adsorption of nanosized palladium catalysts: L_3 edge vs K edge X-ray absorption spectroscopy. *J. Phys. Chem. C* **113**, 15140–15147 (2009).
48. Richardson, T. J. et al. X-ray absorption spectroscopy of transition metal-magnesium hydride thin films. *J. Alloys Compd.* **356–357**, 204–207 (2003).
49. Harris, J. J., Jolivet, R. & Attwell, D. Synaptic energy use and supply. *Neuron* **75**, 762–777 (2012).
50. Katase, T., Onozato, T., Hirono, M., Mizuno, T. & Ohta, H. A transparent electrochromic metal-insulator switching device with three-terminal transistor geometry. *Sci. Rep.* **6**, 25819 (2016).

Acknowledgements

Author contributions

A.J.T. and G.S.D.B. conceived and designed the experiments. G.S.D.B. supervised the project. H.L.T. provided insight into the reaction processes and mechanisms. A.J.T. fabricated the samples with assistance from M.H. C.O.A. and A.J.T. conducted the anomalous and planar Hall measurements. F.B., W.H., C.M. and A.J.T. performed the XAS measurements. S.W. provided insights on the XAS data. A.J.T. performed the MOKE measurements with help from M.M. A.J.T. wrote the manuscript with guidance from H.L.T and G.S.D.B. All authors discussed the results.

Competing Interests

The author declares no competing interests.

Additional information

Methods

Sample preparation. Ta(4 nm)/Pt(3 nm)/Co(0.9 nm)/GdO$_x$(t_{GdO_x} (nm))/Au(3 nm) films were fabricated on thermally oxidized Si (100) substrates using magnetron sputtering at room temperature and 3 mTorr Ar pressure. The metal layers were grown by direct-current sputtering. The GdO$_x$ layer was deposited either using reactive sputtering with p_{O_2} of 0.07 mTorr or radio-frequency sputtering with p_{O_2} of 0.7 mTorr O$_2$. For the samples described in Fig. 1 with Co in the initially oxidized state, the Co layer was reactively sputtered with p_{O_2} of 0.07 mTorr O$_2$ with a deposition time corresponding to the time required to deposit 0.9 nm of metallic Co. For AHE and PHE measurements, the structure is patterned into a Hall cross geometry with 500 µm arm width and with Au(3 nm) deposited over the 0.25 mm^2 active region to serve as a gate electrode. For MOKE measurements, 200-µm diameter Au(3 nm) electrodes were patterned on top of the GdO$_x$ layer of a continuous film, with the Ta(4 nm)/Pt(3 nm) underlayer uncovered by GdO$_x$ at the sample edge to allow electrical contact to the back. All patterning was done using shadow mask lithography. The measured leakage current in the GdO$_x$ films is <1 nA at $V_G = +2$ V for devices with diameter 200 µm and 30-nm-thick GdO$_x$.

Hall effect measurements in different atmospheres. Anomalous Hall effect (AHE) and planar Hall effect (PHE) measurements were performed using a lock-in amplifier with an alternating-current injected current of amplitude 2 mA and frequency 1 kHz. For the AHE measurements, the field was swept perpendicular to the plane; for the PHE measurements, the field was oriented in the sample plane, at 45° to the current flow axis. AHE and PHE hysteresis loops were acquired using a 2-s field sweep time. The measurements were performed in a modified CVX-PF Lakeshore probe station with a base vacuum pressure of about 10^{-4} mbar.

Experiments under controlled gas environments were performed by backfilling the chamber with either O$_2$ gas (99.999% purity) or N$_2$ gas (99.999% purity). Humidity was introduced into the N$_2$ gas flow by bubbling through water. Wet N$_2$ and ambient conditions at 25 °C correspond to about 20 mtorr and 12 mtorr of H$_2$O partial pressure respectively. All experiments were performed at room temperature.

Polar MOKE measurements. MOKE measurements were performed using a 1-mW laser with a wavelength of 660 nm focused to a spot size of about 10 µm. Experiments were performed in polar geometry and hence sensitive to the out-of-plane magnetization component. To apply gate voltage V_G to the circular electrodes, a CuBe probe was placed near the edge of the electrode and the Ta/Pt back electrode was grounded. The laser spot was focused on the middle of the electrode. All experiments were performed at room temperature.

XAS. XAS spectra were acquired at the Coherent Soft X-ray Scattering beamline at the National Synchrotron Light Source II, Brookhaven National Laboratory using fluorescent yield. The incident soft X-ray beam has a footprint of about 200 µm and the sample is tilted 15° relative to the incident beam. The sample used for the measurement has a Hall bar geometry with sample structure Ta(4 nm)/Pd(3 nm)/Co(0.6 nm)/Pd(4.5 nm)/GdO$_x$ (30 nm) and a 3 nm Au top gate. The main chamber base pressure is about 2×10^{-9} torr, and the sample is kept at 100 K throughout the measurement.

Data availability

The data that support the findings of this study are available from the corresponding author upon reasonable request.